ARTICLE OPEN ACCESS

Ant-Nest Corrosion in Copper Pipes Triggered by Ethylene Vinyl Acetate-Based Adhesive

Luca Cozzarini[1] | Lucia Marsich[2] | Alessio Ferluga[2]

[1]Department of Engineering and Architecture, University of Trieste, Trieste, Italy | [2]MaterialScan Srl, Trieste, Italy

Correspondence: Luca Cozzarini (lcozzarini@units.it)

Received: 16 July 2024 | **Accepted:** 17 September 2024

Funding: The authors received no specific funding for this work.

Keywords: ant-nest corrosion | copper pipes | heat exchanger | optical microscopy | scanning electron microscopy

ABSTRACT

Corrosion of condenser circuits in refrigeration systems significantly impacts appliance reliability and longevity. This study investigates an unreported cause linked to changing adhesive materials during copper pipe assembly. Transitioning from a polyethylene-based adhesive to one containing ethylene vinyl acetate caused unexpected perforation of copper coils within months. We hypothesized that even trace amounts of acetic acid, a byproduct of the latter adhesive, trigger a peculiar localized morphology known as "ant-nest corrosion." We propose using ethylene vinyl acetate-free adhesives to prevent this issue in refrigeration systems.

1 | Introduction

Copper, valued for its excellent thermal conductivity, is widely used in heat exchanger systems like radiators, condensers, evaporators, and air conditioning units [1–4]. The leaking failure of copper pipes in heat exchangers due to pitting corrosion has long been recognized as a critical issue impacting appliance performance and service life. This corrosion type poses particular challenges in diagnosis and prevention, often resulting in leakages and premature failures of thin-walled copper tubing in heat exchangers [5–10]. A manufacturer of compact refrigerators based in northern Italy reported instances of premature failure in certain units shortly after being put into service, typically occurring within 1–2 years. According to their documentation, this is notably shorter than the expected standard durability of a decade for appliances of this type. The failure occurs due to refrigerant leakage from the circuit. Upon disassembly of the circuit, the leakage area, following pressure tests, was identified in the copper coils of the heat exchanger located at the back of the fridge. The leaks occur from microscopic holes in the coil tubes, initially invisible to the naked eye, identified as a peculiar form of localized corrosion known as "ant-nest" or "formicary" corrosion. It has been speculated that this form of corrosion, first described in the late '70s [11], contributes to approximately 10% of copper heat exchanger failures worldwide [1, 7, 12–15]. The corrosion pattern is characterized by microscopic tunnels (not noticeable by naked eye observation) that propagate randomly inside the tube wall, forming interconnecting longitudinal networks similar to a formicary when observed in cross-section [9, 12, 14, 16]. The rapid corrosion rate, estimated at 10 μm per day at 0.3 mA cm^{-2}, along with the random propagation of these tunnels through the tube wall, underscores the severity of the issue [15, 17, 18]. Corrosion products, primarily comprising copper (I) oxide, may be transported along the tube surface. The initiation of ant-nest corrosion in copper tubes is commonly associated with the simultaneous presence of air, moisture, and carboxylic acids [7–11], originating from various sources such as residual organic compounds, anthropogenic or biogenic processes, or the decomposition of paints or hemicellulose in wood, among others [11–14]. The accepted corrosion mechanism involves carboxylic acids attacking the patina covering the copper surface, comprised mainly of cupric oxides/hydroxides. Unstable cuprous carboxylate complexes and cuprous oxide are formed

in the localized corrosion areas. Subsequent volume expansion from deposited cuprous oxide leads to microcrack formation, exposing additional copper surfaces to the corrosive environment. The refrigerator pipes were assembled manually using hot melt glue. Subsequently, they were encapsulated with expanded polyurethane foam for thermal insulation purposes. The manufacturer reports that the premature leaking affects units bonded with a specific type of hot melt glue (referred to as adhesive A), while it does not seem to affect units assembled with an adhesive of similar performance but purchased from another supplier (referred to as adhesive B). While various factors contribute to this particular corrosion morphology, the role of adhesive materials during assembly has not received attention in the literature. This study highlights the critical interplay between materials selection, assembly techniques, and corrosion susceptibility in refrigeration systems, aiming to elucidate underlying mechanisms and propose effective mitigation strategies to preserve equipment integrity and functionality.

2 | Materials and Methods

The copper tubes (outer diameter 8 mm, wall thickness 0.6 mm) were cut from a damaged heat exchanger supplied by the refrigerator manufacturer. According to the technical datasheet, the tubes are made of deoxidized high-phosphorus copper (Cu-DHP, Cu $\geq$ 99.9%, P content between 0.015% and 0.04%), equivalent to C12200 (ASTM B111-98 designation [19]) or CW024A (EN 12451 designation [20]). A certificate issued by the material manufacturer confirmed the compliance with the declared grade (Cu = 99.96%; $p = 0.03\%$). A pressure test was conducted to identify leakage points in the failed tubes. One end of the cut tube sample was connected to an air compressor (Polar KWU550-8L), and the other end was sealed. The sample was pressurized to 3 bar and submerged in a water tank. Bubbling was observed to pinpoint the exact locations of leakage. Subsequently, sections adjacent to the identified leakage points were cut into cross-sectional and longitudinal sections for further metallographic analysis. Samples for metallography were embedded in a transparent methyl methacrylate-based resin and polished according to ASTM E3-11 standard, tab. 7 [21], and then analyzed under optical and electron microscope. Optical microscopy (OM) images were collected by a Nikon Eclipse 50i and by a portable microscope DinoLite AM4515ZT. Scanning electron microscopy (SEM) investigation was performed by a Zeiss Gemini 300 FEG operating at 20 kV accelerating voltage, equipped with a Pentafet Plus detector for energy dispersive spectrometry (EDS) analysis; secondary electron (SE) detector was a Everhart-Thornley SE detector with optically coupled photomultiplier; backscattered electron (BSE) detector a Zeiss 6-segment aBSD4 detector. Raman spectra of corrosion products were collected with a Renishaw InVia Raman Microscope equipped with a RenCam CCD detector, operated by a Renishaw Wire 3.2 software. Excitation source was a Toptica XTRA II 500 mW diode laser ($\lambda = 785$ nm). X-ray diffraction (XRD) patterns of the pipe external patina were recorded on a Bruker D5005 diffractometer operating at 40 kV/20 mA using Cu Kα ($E = 8.04$ keV; $\lambda = 1.5406$ Å), over a $10° < 2\theta < 70°$ angular range (angular resolution: 0.05°; time/step: 4 s). Samples of the two hot melt adhesives

FIGURE 1 | Failed pipe section as cut (A) and the same failed pipe section during the pressure test (B). The exact location of leakage due to microscopic holes (not visible in A) is pinpointed by the air bubbles in B. [Color figure can be viewed at wileyonlinelibrary.com]

(according to the manufacturer, an ethylene vinyl acetate-based adhesive, identified as "adhesive A" and a polyethylene-based one, identified as "adhesive B") were provided by the refrigerator manufacturer and were analyzed and identified using Fourier-transform infrared spectroscopy (FT-IR). FT-IR spectra were collected with a Shimadzu IR Spirit spectrometer equipped with an attenuated total reflectance (ATR) accessory, covering the spectral range of 4000–500 cm^{-1}. In addition to automatic identification performed by the software (Shimadzu LabSolution IR database), vibrational bands were also cross-referenced with known reference spectra in the literature.

3 | Results

The picture of a representative failed section of the pipe is depicted in Figure 1. Figure 1A shows the failed pipe section after being cut, while Figure 1B displays the same sample during the pressure test. In Figure 1A, the microscopic holes are imperceptible to the naked eye. On the other hand, in Figure 1B, the presence of air bubbles during the pressure test pinpoints the exact location of leakage. These bubbles highlight the previously unseen microscopic holes, emphasizing the importance of the pressure test in identifying the leakage location. The tube surfaces display characteristic copper patinas, exhibiting both dark-blueish and dark-red variants, as illustrated in Figure 2A,B. These patinas are typically composed of various copper compounds [5, 22]. Usually, among these, copper (II) oxide (CuO or tenorite) appears dark in color, and copper basic carbonate, a mixture of $Cu_2(OH)_2CO_3$ (malachite) and $Cu_3(OH)_2(CO_3)_2$ (azurite) appear green to blue. Additionally, copper (I) oxide (Cu_2O or cuprite) contributes to dark red to bright-red hues. Bright blue deposit could be identified as azurite or as copper (II) acetate ($Cu(COOH)_2$), adding further complexity to the corrosion products observed. Raman spectroscopy conducted on the pipe surface (Figure 3A,B) unveiled distinctive Cu (I) oxide signals, including characteristic shifts at 148 and 220 cm^{-1} [23–27]. The detection of Cu (II) oxide signals (Figure 3C), represented by a peak at 296 cm^{-1} [23, 24, 27–29]) was sporadic and limited to certain dark areas, and only after laser-induced overheating. No characteristic signals of carbonates/hydroxides were discerned on the patina [29]. It is

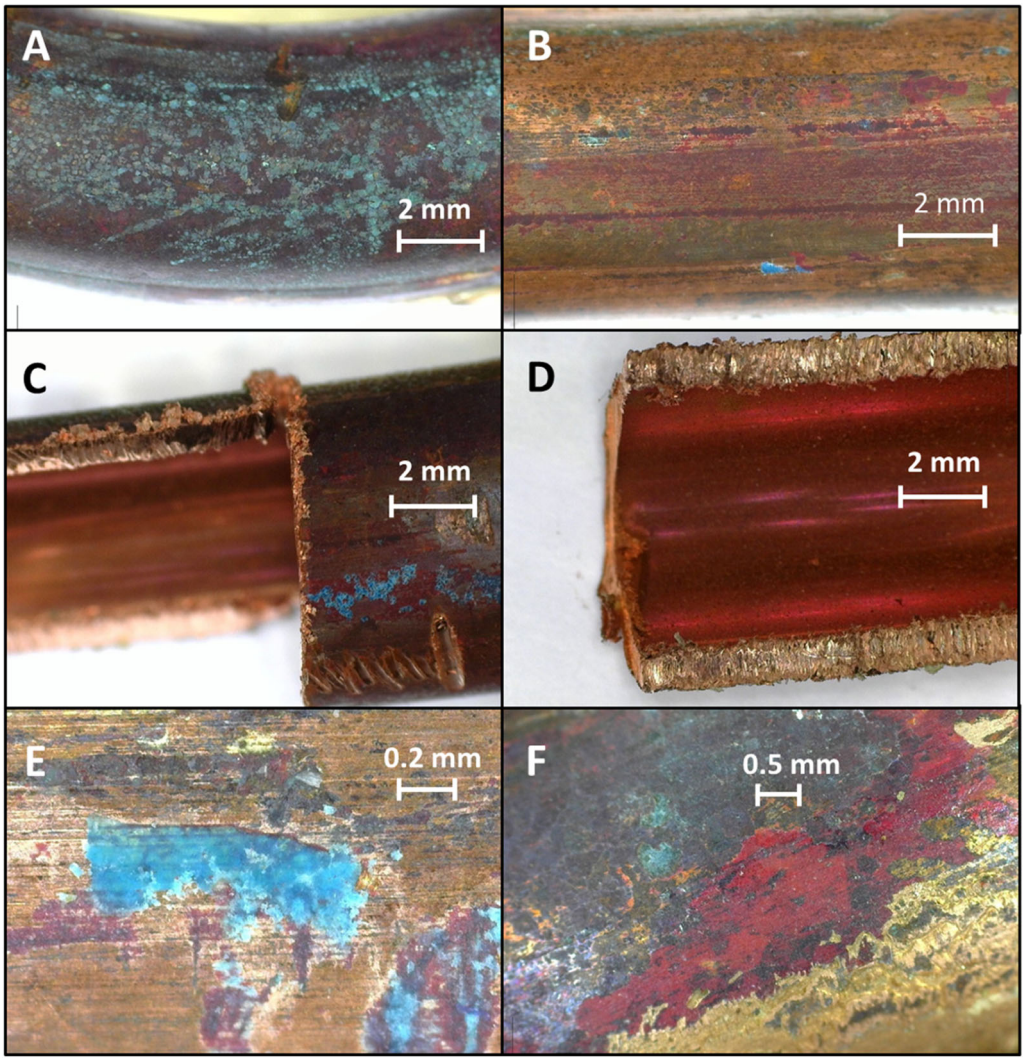

FIGURE 2 | Low magnification micrographs of samples: (A) example of dark/blueish patina; (B) example of dark red patina; (C) area next to sample cutting: dark patina and bright blue deposits on the outside, copper with no patina on the inside; (D) inner surface of the tube, no deposits or evident patina; (E) details of a bright blue deposit; (F) details of a bright red deposit next to a dark patina. [Color figure can be viewed at wileyonlinelibrary.com]

recognized that Cu (I) oxide thin films, formed adjacent to the metal surface, may exhibit dark or brown-black tones, differing from the typical red hue of bulk cuprite mineral [30]. XRD analysis (Figure 4) confirmed the presence of a cuprite layer on the outer pipe surface, with a minor diffraction signal attributed to malachite [26, 27, 31]. Furthermore, Raman spectroscopy conducted on selected blue regions (Figure 3D) exhibited signals consistent with malachite, characterized by a Raman shift at 430 cm^{-1} [31–33]. Interestingly, the inner surfaces of the tubes, as depicted in Figure 2C,D, appear unpatinated. Upon closer examination, Figure 2E,F provides detailed views of bright blue and bright red deposits. Further analysis with a portable optical microscope in Figure 5 revealed the presence of pits along the lateral edges, particularly in areas immediately adjacent to the hot melt adhesive. Figure 5A captures an area adjacent to the adhesive before removal, while Figure 5B shows the same area post-adhesive removal. Magnified views in Figure 5C–F shows numerous pits (highlighted by red arrows), indicative of localized corrosion phenomena. Intense blue and bright red corrosion products are observed both inside and adjacent to most pits. In Figure 6A,C, two representative images of the cross-section of the tube are depicted, while the longitudinal sections are shown in Figure 6B,D. Evidently, the presence of pits originating from the outer surface of the tube is observable, manifesting as microscopic tunnels randomly traversing the tube wall, extending longitudinally. Subsequently, these tunnels breach the inner surface of the tube (Figure 6D), resulting in perforation and gas leakage. Similar phenomena are observed in the cross-sectional views. Notably, the interconnected nature of multiple galleries is apparent in Figure 6C, where smaller cavities converge into larger tunnels (Figure 7).

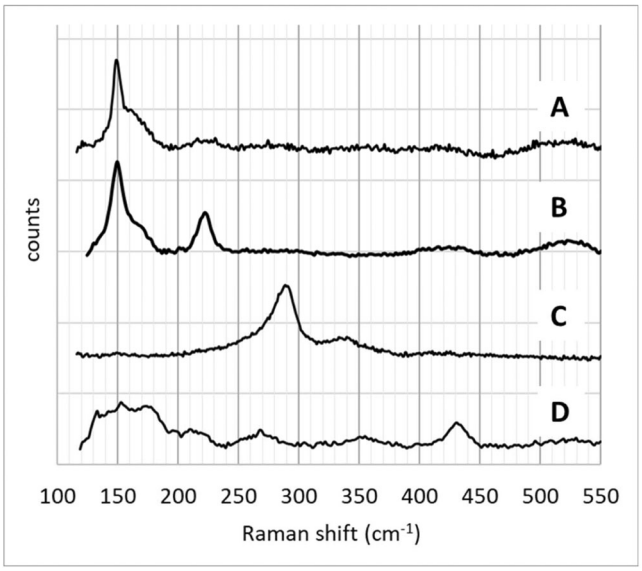

FIGURE 3 | Raman spectra of (A) dark patina; (B) red spot; (C) overheated dark spot; (D) blue spot.

Figures 8 and 9 illustrate the details of two pits developing perpendicular to the longitudinal section of the tubes. These pits, visible in both SEM images acquired with SEs (A) and BSEs (B), exhibit contrasting topographic and atomic number characteristics, respectively. The brighter regions in the BSE image (B) indicate areas with higher atomic number elements, such as metallic copper. BSE in SEM imaging provide contrast related to atomic number because higher atomic number elements tend to scatter electrons more effectively than lower atomic number elements. As a result, regions with higher atomic number elements appear brighter in BSE images. Copper has a higher atomic number than other elements typically found in corrosion products, such as oxides. Therefore, areas containing copper will appear brighter in BSE images due to the higher atomic number contrast, while areas with corrosion products will appear darker because they typically have a lower average atomic number compared to the original metal. Additionally, an EDX map of oxygen distribution superimposed onto the SEM image highlights the

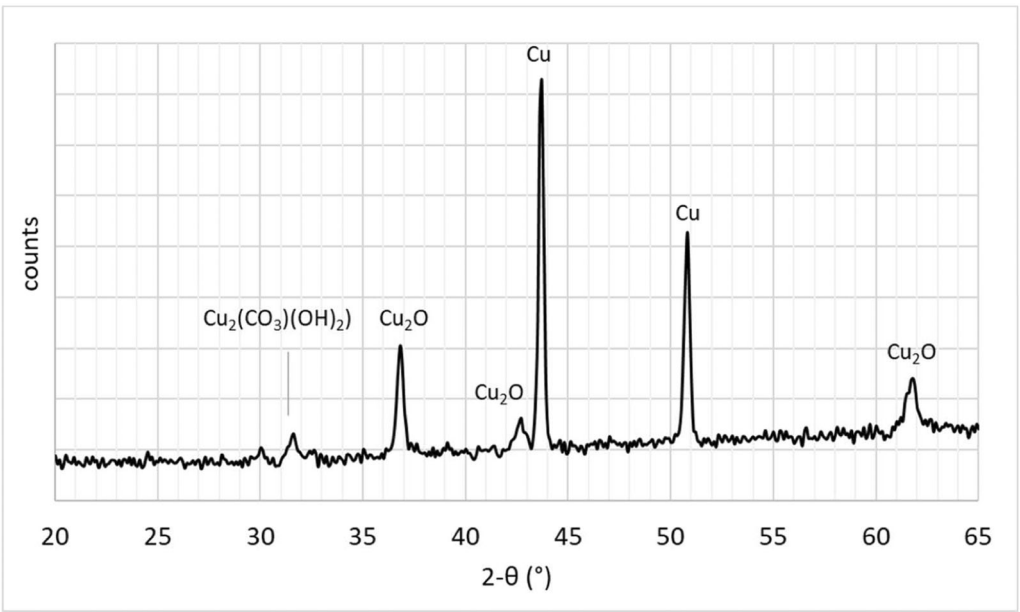

FIGURE 4 | X-ray diffractogram of the pipe's external patina.

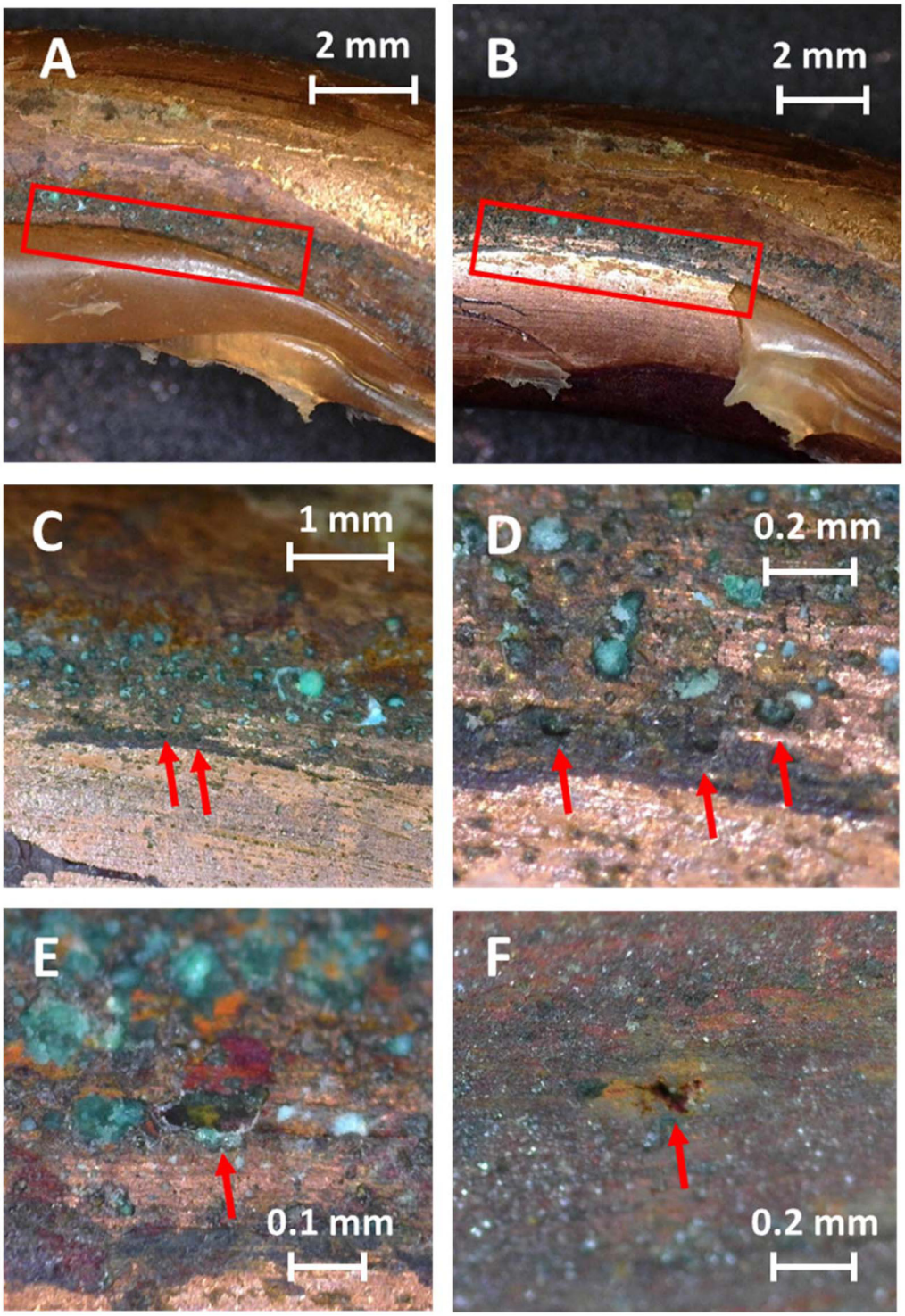

FIGURE 5 | Low magnification micrographs of samples: (A) area next to the hot adhesive, prior to adhesive removal; (B) same area, after adhesive removal. (C) and (D): magnification of the area highlighted in (B), several pits can be noticed. (E) details of one pit: blue and bright red corrosion products can be spotted. (F) details of another pit, no corrosion products. [Color figure can be viewed at wileyonlinelibrary.com]

distribution of oxygen within the pits. These oxygen-rich areas correspond to regions where corrosion products, such as oxides or hydroxides, develop. Therefore, the EDX map of oxygen distribution serves as a complementary technique to the BSE imaging, providing additional confirmation of the presence of corrosion products in the darker regions of the image. This combined approach helps to validate the interpretation of the BSE image and provides further insights into the distribution and composition of corrosion products inside the pipe section.

In Figure 10A, the FT-IR spectrum of the thermoplastic adhesive "A" is shown. The spectrum exhibits characteristic vibrational bands associated with the functional groups present in ethylene-vinyl acetate (EVA) [34–37]. Aliphatic and vinyl C-H stretching are observed at 2850, 2917, and 2950 cm^{-1}. Carbonyl

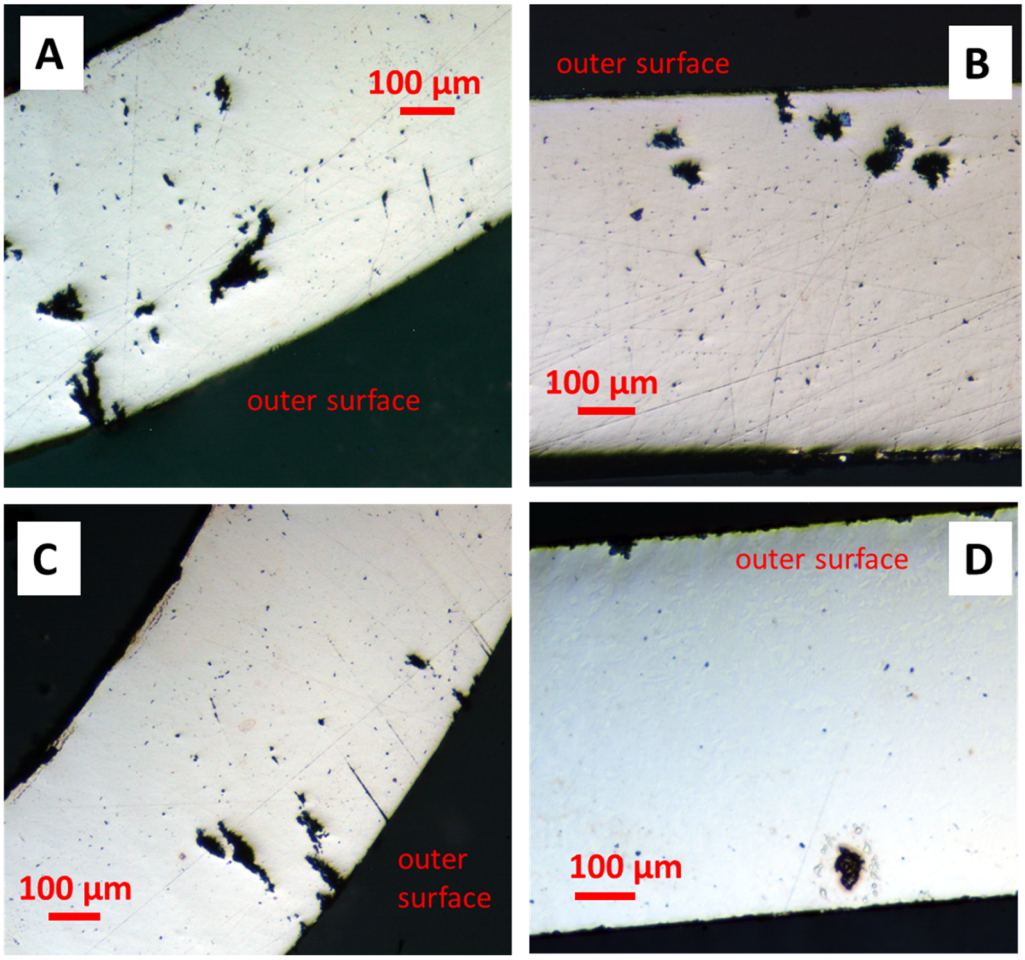

FIGURE 6 | Metallographic micrographs of samples: cross sections (A, C); longitudinal sections (B, D). [Color figure can be viewed at wileyonlinelibrary.com]

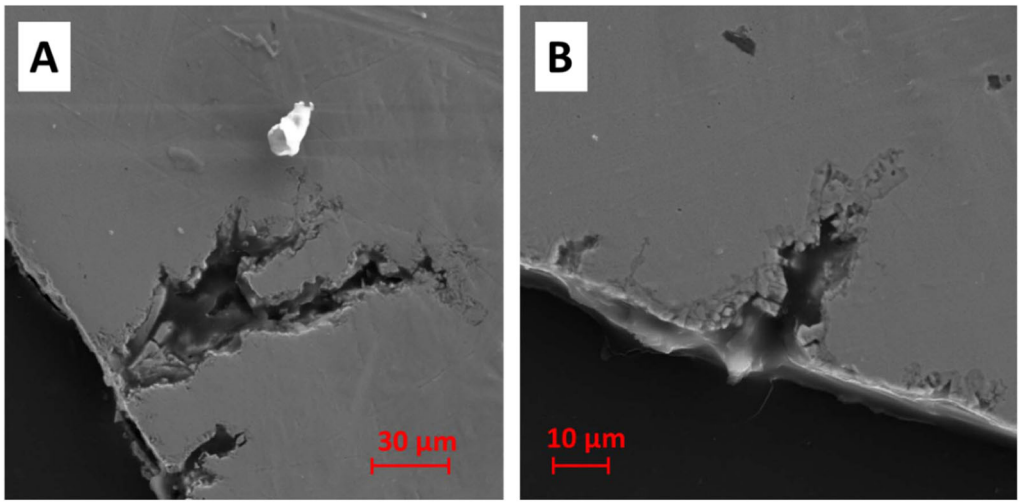

FIGURE 7 | SEM images: details of pits originating from the outer surface of the cross-sections of the tubes. [Color figure can be viewed at wileyonlinelibrary.com]

(C═O) stretching can be noticed at 1739 cm^{-1}; methylene (CH_2) bending at 1466 cm^{-1}; methyl bending (CH_3) at 1371 cm^{-1}; vinyl acetate (C═O) and ester (C–O–C) stretching at 1238 and 1020 cm^{-1}; vinyl (CH_2═CH) bending at 719 cm^{-1}. Also, the Shimadzu FTIR database [38] identified the adhesive "A" spectrum as EVA. In Figure 10B, the FT-IR spectrum of the thermoplastic adhesive "B" is shown. The spectrum exhibits most of the characteristic vibrational bands associated with the functional groups present in polypropylene (PP) and polyethylene (PE) [34, 35, 39, 40]. Aliphatic stretching are observed

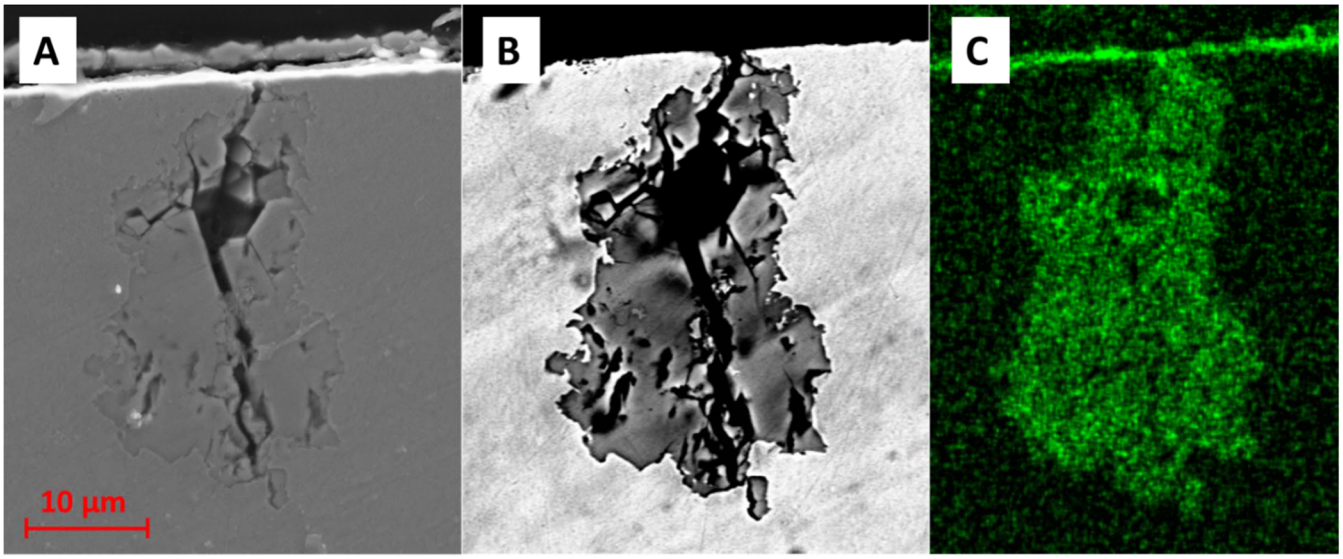

FIGURE 8 | Details of a pit originating from the outer surface of the longitudinal section of the tubes. (A) SEM image acquired with secondary electrons (topographic contrast); (B) SEM image acquired with backscattered electrons (atomic number contrast); (C) EDX map of oxygen distribution superimposed onto the SEM image. [Color figure can be viewed at wileyonlinelibrary.com]

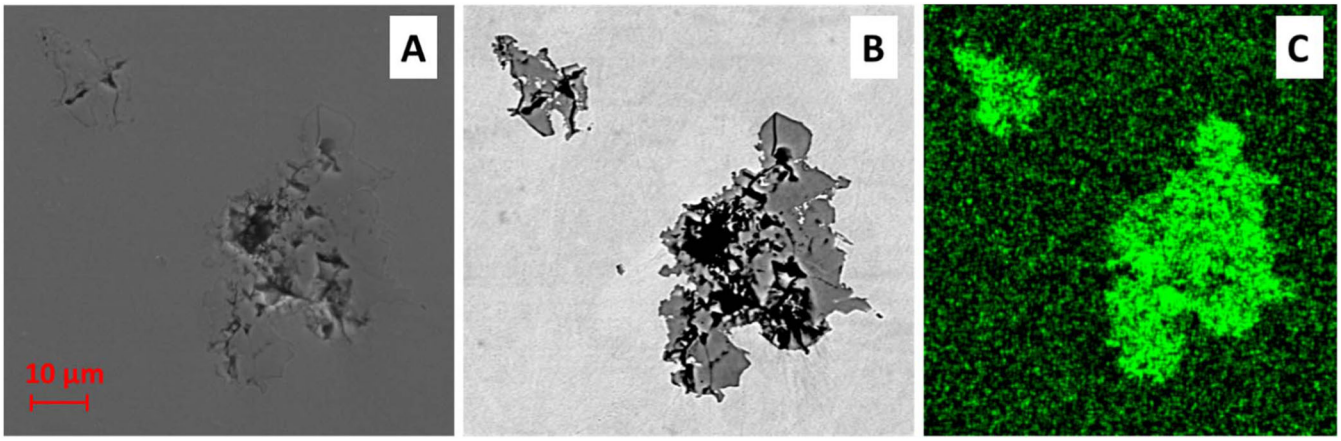

FIGURE 9 | Details of two pits developing perpendicularly to the longitudinal section of the tubes. (A) SEM image acquired with secondary electrons (topographic contrast); (B) SEM image acquired with backscattered electrons (atomic number contrast); (C) EDX map of oxygen distribution superimposed to SEM image. These oxygen-rich areas correspond to regions where corrosion products (oxides or hydroxides) have formed. [Color figure can be viewed at wileyonlinelibrary.com]

in the 2850–2950 cm^{-1} range; methylene (CH_2) bending at 1459 cm^{-1}; methyl bending (CH_3) at 1375 cm^{-1}; C–H stretch in methyl groups at 1231 cm^{-1}; CH_2 rocking at 972 cm^{-1}. The Shimadzu FTIR database [38] identified the adhesive "B" spectrum as a polyolefin (PP/PE)-based polymer, with the presence of minor additives (that can be related to other minor vibrational bands, such that visible at 1537 cm^{-1}). Peaks related to EVA are not recorded in adhesive "B."

4 | Discussion

The pressure test on the examined pipes revealed numerous leaks from the side adjacent to the hot melt adhesive; this area shows numerous pits not visible to the naked eye filled with bright blue and red deposits, identified as copper basic carbonate and copper (I) oxide, respectively. The inner surface shows no deposits and the pits are less visible. The pits propagate from the outer surface of the tube and develop randomly within the wall, even longitudinally, before reaching the inner surface of the tube causing perforation and refrigerant leaking. This form of corrosion, defined as ant-nest corrosion due to its morphology, is linked to the presence of oxygen, moisture, and carboxylic acids, such as acetic acid, even at low concentrations [7, 14, 16, 18, 41]. FT-IR spectroscopy revealed that the hot melt adhesive "A" is composed of EVA. If heated, EVA can release acetic acid already at temperatures between 105°C and 180°C [42]. The initiation of copper coil corrosion is therefore due to the presence of acetic acid released by the adhesive in the EVA. A generally accepted mechanism of ant-nest corrosion involves several steps [14, 15, 18, 43]. Typically, copper in the atmosphere is passivated by a protective patina composed of a mixture of copper carbonates, hydroxides, and

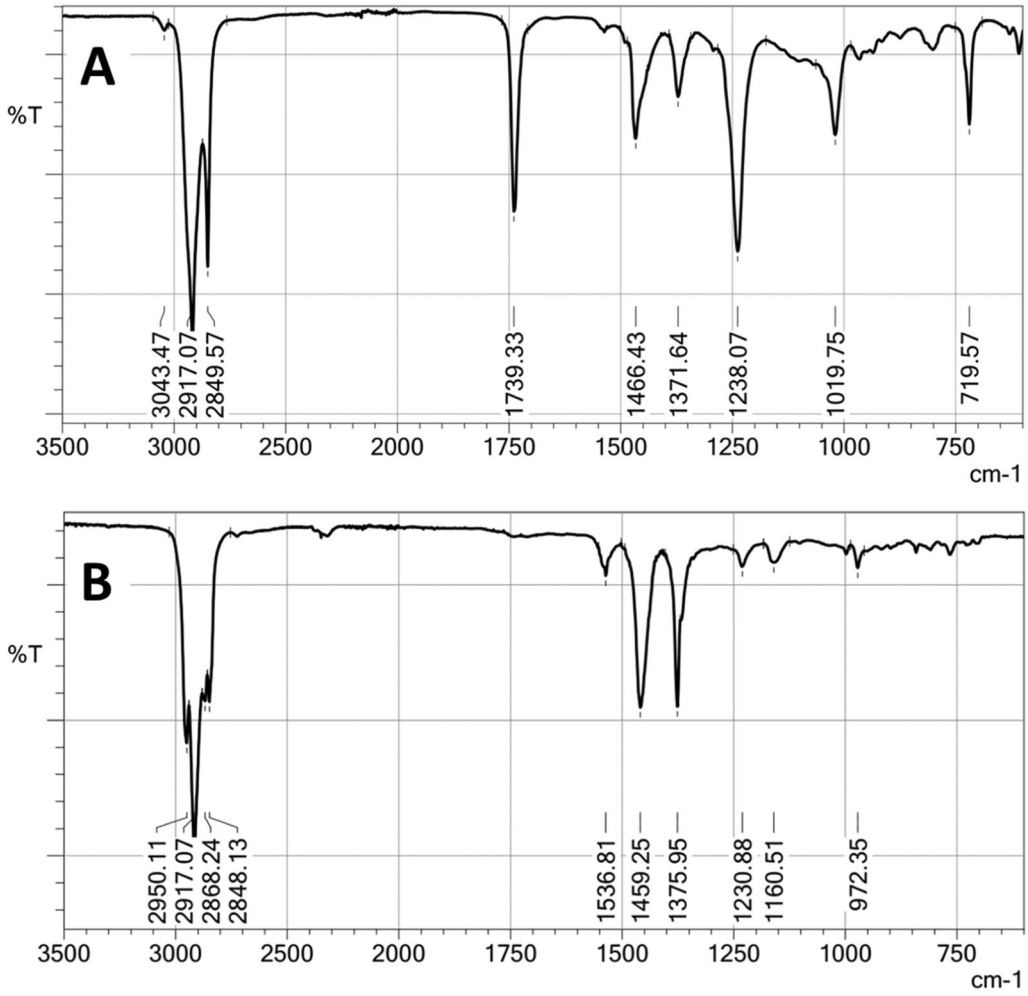

FIGURE 10 | FT-IR spectra of the thermoplastic adhesive "A" and "B."

oxides [22, 44]. It is widely accepted that the passive film formed on the surface of copper consists of a dual-layer structure, with a less protective Cu (I) oxide layer adjacent to the metal and an external Cu (II) oxide (or hydroxide, basic carbonate, or a combination of these) that acts as a protective layer [1, 5, 44]. In the examined case, the patina was found to be mainly composed of Cu (I) oxide, covering most of the pipe's outer surfaces. The observation of signals consistent only with this latter compound does not definitively rule out the presence of other compounds in the surface patina. The cuprite layer, which develops in direct contact with the metal, might be dense and crystalline, unlike other compounds such as carbonates, acetates, or hydroxides, which may not exhibit crystallinity or stoichiometry, thereby potentially escaping detection through diffraction or Raman spectroscopy. The outer layer of the patina can be compromised in the presence of carboxylic acids, such as acetic acid, that can form soluble compounds like copper acetate [41, 45]. This damage to the protective patina can expose the underlying metal to the corrosive action, triggering localized corrosion morphologies in the form of microscopic pits. In oxygen-deficient environments, eased by the presence of copper acetate, Cu (I) oxide can develop

$$2Cu(CH_3COO)_2 + H_2O + 2e^- \rightarrow Cu_2O + 2CH_3COOH + 2CH_3COO^-, \quad (1)$$

$$2Cu + H_2O \rightarrow Cu_2O + 2H^+ + 2e^-. \quad (2)$$

Notably, this oxide possesses a molar volume roughly double that of Cu (II) oxide. The volume expansion resulting from the deposited Cu (I) oxide within the pits induces a wedging effect, leading to the creation of microcracks that expose more copper surface to the corrosive environment. This, in turn, facilitates the further formation of Cu acetate and Cu (I) oxide. Once initiated, ant-nest corrosion becomes a self-sustaining process, with the described reactions repeating until tunnels propagate through the walls, eventually resulting in pipe leakage failure.

5 | Conclusions and Prevention Measures

Based on the analyses conducted, the following conclusions have been drawn:

- A failure analysis was conducted on copper pipes sourced from the refrigerator condenser circuit.
- Experimental observations revealed characteristic features consistent with the mechanism of ant-nest corrosion.
- It was demonstrated that the initiation of an ant-nest corrosion attack could be attributed to the use of hot melt

adhesive containing EVA, which releases acetic acid upon heating during the glueing process.

This failure underscores the critical yet unexpected role of adhesive selection in copper pipe corrosion. The refrigerator pipes were assembled manually using hot melt glue; the premature leaking affects units bonded with a specific type of adhesive containing ethylene vinyl acetate, while units assembled with another adhesive of similar performance but different chemical formulations seem unaffected. Despite the seemingly innocuous substitution of a conventional polyethylene-based adhesive with one containing ethylene vinyl acetate, the consequences were significant. The latter adhesive unexpectedly triggered a relatively rapid corrosion event and finally the failure due to the leaking of the condenser circuit within the refrigeration system. It is worth noting that the typical timeframe for an ant-nest corrosion failure is on the order of several months, rather than years as reported in this case. In this specific instance, although the failure occurred before the forecasted time of appliance operation, it can be speculated that the arrival of atmospheric humidity on the pipe surface may have been hindered or delayed by the PU foam encapsulation. Additionally, it can also be hypothesized that the concentration of acetic acid resulting from the melting of the hot melt adhesive is lower than in typical reported cases. A recommended preventive measure for addressing this specific failure is to replace the adhesive containing EVA with an alternative adhesive, such as the one based solely on polyolefin.

Acknowledgments

The authors received no specific funding for this work. Open access publishing facilitated by Universita degli Studi di Trieste, as part of the Wiley - CRUI-CARE agreement.

Data Availability Statement

The data that support the findings of this study are available from the corresponding author upon reasonable request.

References

1. D. M. Bastidas, M. Criado, S. Fajardo, V. M. La Iglesia, E. Cano, and J. M. Bastidas, "Copper Deterioration: Causes, Diagnosis and Risk Minimisation," *International Materials Reviews* 55 (2010): 99–127, https://doi.org/10.1179/095066009X12506721665257.

2. K. Chandra, V. Kain, P. S. Shetty, and R. Kishan, "Failure Analysis of Copper Tube Used in a Refrigerating Plant," *Engineering Failure Analysis* 37 (2014): 1–11, https://doi.org/10.1016/j.engfailanal.2013.11.014.

3. L. Fedrizzi, F. Deflorian, and P. Bonora, "Evaluation of the Protective Properties of Organic Coatings on Copper Pipes for Refrigerator Cooling Circuit," *Electrochimica Acta* 44 (1999): 4251–4258, https://doi.org/10.1016/S0013-4686(99)00140-1.

4. L. Fedrizzi, F. Andreatta, L. Paussa, F. Deflorian, and S. Maschio, "Heat Exchangers Corrosion Protection by Using Organic Coatings," *Progress in Organic Coatings* 63 (2008): 299–306, https://doi.org/10.1016/j.porgcoat.2008.01.009.

5. A. Cohen, "Corrosion of Copper and Copper Alloys," in *Corrosion: Materials*, eds. S. D. Cramer and B. S. Covino Jr. (Materials Park, OH, USA: ASM International Digital Library, 2005), https://doi.org/10.31399/asm.hb.v13b.a0003816.

6. J. Gibson and B. Karney, "A 30-Year Review of Copper Pitting Corrosion and Pinhole Leaks: Achievements and Research Gaps," *AWWA Water Science* 3 (2021): e1221, https://doi.org/10.1002/aws2.1221.

7. F. Sargın, K. Kanbur, and İ. Türkmen, "Failure Analysis of Copper Pipes Used in the Heat Exchangers in Fan Coil Units," *Revista de Metalurgia* 59 (2023): e239, https://doi.org/10.3989/revmetalm.239.

8. B. Kuźnicka and K. Junik, "Intergranular Stress Corrosion Cracking of Copper: A Case Study," *Corrosion Science* 49 (2007): 3905–3916, https://doi.org/10.1016/j.corsci.2007.05.014.

9. H. Peltola and M. Lindgren, "Failure Analysis of a Copper Tube in a Finned Heat Exchanger," *Engineering Failure Analysis* 51 (2015): 83–97, https://doi.org/10.1016/j.engfailanal.2015.02.016.

10. W. Faes, S. Lecompte, Z. Y. Ahmed, et al., "Corrosion and Corrosion Prevention in Heat Exchangers," *Corrosion Reviews* 37 (2019): 131–155, https://doi.org/10.1515/corrrev-2018-0054.

11. J. O. Edwards, R. I. Hamilton, and J. B. Gilmour, "Early Corrosion Failures in Copper Heat Exchanger Tubing," *Materials Performance* 16 (1977): 18–20.

12. E. Cano, J. Simancas, J. L. Polo, C. L. Torres, J. M. Bastidas, and J. Alcolea, "Early Corrosion Failure of Copper Tubing Used in Air-Conditioning Units," *Materials and Corrosion* 50 (1999): 103–110, https://doi.org/10.1002/(SICI)1521-4176(199902)50:2<103::AID-MACO103>3.0.CO;2-B.

13. T. Notoya, "Localized Corrosion in Copper Tubes and the Effect of Anti-Tarnishing Pretreatment," *Journal of Materials Science Letters* 10 (1991): 389–391, https://doi.org/10.1007/BF00728041.

14. R. S. Situmorang and H. Kawai, "Investigating the Mechanism Behind 'Ant-Nest' Corrosion on Copper Tube," *Materials* 11 (2018): 533, https://doi.org/10.3390/ma11040533.

15. P. Elliott and R. A. Corbett, "Ant-Nest Corrosion—Exploring the Labyrinth," *Corrosion Reviews* 19 (2001): 1–14, https://doi.org/10.1515/CORRREV.2001.19.1.1.

16. D. M. Bastidas, I. Cayuela, and J. M. Bastidas, "Ant-Nest Corrosion of Copper Tubing in Air-Conditioning Units," *Revista de Metalurgia* 42 (2006): 367–381, https://doi.org/10.3989/revmetalm.2006.v42.i5.34.

17. A. Vazdirvanidis, S. Papadopoulou, S. Papaefthymiou, G. Pantazopoulos, and D. Skarmoutsos, "Copper Tubing Failure due to Ant-Nest Corrosion," *MATEC Web of Conferences* 188 (2018): 03005, https://doi.org/10.1051/matecconf/201818803005.

18. M. M. Lachowicz, "A Metallographic Case Study of Formicary Corrosion in Heat Exchanger Copper Tubes," *Engineering Failure Analysis* 111 (2020): 104502, https://doi.org/10.1016/j.engfailanal.2020.104502.

19. "ASTM B111-98—Standard Specification for Copper and Copper-Alloy Seamless Condenser Tubes and Ferrule Stock," ASTM International (2004), https://www.astm.org/b0111-98r04.html.

20. "BS EN 12451:2012 Copper and Copper Alloys. Seamless, Round Tubes for Heat Exchangers," European Standards (2012), https://www.en-standard.eu/bs-en-12451-2012-copper-and-copper-alloys-seamless-round-tubes-for-heat-exchangers/.

21. "ASTM E3-11—Standard Guide for Preparation of Metallographic Specimens," ASTM International (2017), https://www.astm.org/e0003-11r17.html.

22. R. Francis, *The Corrosion of Copper and Its Alloys: A Practical Guide for Engineers* (Houston, TX, USA: NACE International, 2010).

23. P. Colomban, A. Tournié, M. Maucuer, and P. Meynard, "On-site Raman and XRF Analysis of Japanese/Chinese Bronze/Brass Patina—

The Search for Specific Raman Signatures," *Journal of Raman Spectroscopy* 43 (2012): 799–808, https://doi.org/10.1002/jrs.3095.

24. Y. Deng, A. D. Handoko, Y. Du, S. Xi, and B. S. Yeo, "*In Situ* Raman Spectroscopy of Copper and Copper Oxide Surfaces During Electrochemical Oxygen Evolution Reaction: Identification of Cu^{III} Oxides as Catalytically Active Species," *ACS Catalysis* 6 (2016): 2473–2481, https://doi.org/10.1021/acscatal.6b00205.

25. M. M. Mennucci, M. Sanchez-Moreno, I. V. Aoki, et al., "Local Electrochemical Investigation of Copper Patina," *Journal of Solid State Electrochemistry* 16 (2012): 109–116, https://doi.org/10.1007/s10008-010-1290-7.

26. "RRUFF Project Database, Cuprite Mineral Data (R050384)," (2024), https://rruff.info/cuprite/display=default/.

27. B. Lafuente, R. T. Downs, H. Yang, and N. Stone, "The Power of Databases: The RRUFF Project," in *Highlights in Mineralogical Crystallography*, eds. T. Armbruster and R. M. Danisi (Berlin, Germany: De Gruyter (O), 2015), 1–30, https://doi.org/10.1515/9783110417104-003.

28. "RRUFF Project Database, Tenorite Mineral Data (R060978)," (2024), https://rruff.info/tenorite/display=default/.

29. R. L. Frost, "Raman Spectroscopy of Selected Copper Minerals of Significance in Corrosion," *Spectrochimica Acta Part A: Molecular and Biomolecular Spectroscopy* 59 (2003): 1195–1204, https://doi.org/10.1016/S1386-1425(02)00315-3.

30. C. Leygraf, T. Chang, G. Herting, and I. Odnevall Wallinder, "The Origin and Evolution of Copper Patina Colour," *Corrosion Science* 157 (2019): 337–346, https://doi.org/10.1016/j.corsci.2019.05.025.

31. "RRUFF Project Database, Malachite Mineral Data (R050531)," (2024), https://rruff.info/malachite/display=default/.

32. M. Bouchard and D. C. Smith, "Catalogue of 45 Reference Raman Spectra of Minerals Concerning Research in Art History or Archaeology, Especially on Corroded Metals and Coloured Glass," *Spectrochimica Acta Part A: Molecular and Biomolecular Spectroscopy* 59 (2003): 2247–2266, https://doi.org/10.1016/S1386-1425(03)00069-6.

33. S. Pagano, G. Balassone, C. Germinario, et al., "Archaeometric Characterisation and Assessment of Conservation State of Coins: The Case-Study of a Selection of Antoniniani From the Hoard of Cumae (Campania Region, Southern Italy)," *Heritage* 6 (2023): 2038–2055, https://doi.org/10.3390/heritage6020110.

34. G. Socrates, *Infrared and Raman Characteristic Group Frequencies: Tables and Charts*, 3rd ed. (Hoboken, NJ, USA: John Wiley & Sons Inc., 2004).

35. P. Larkin, *Infrared and Raman Spectroscopy*, 1st ed. (Amsterdam, Netherlands: Elsevier, 2011).

36. "ASTM D5594-98—Standard Test Method for Determination of the Vinyl Acetate Content of Ethylene-Vinyl Acetate (EVA) Copolymers by Fourier Transform Infrared Spectroscopy (FT-IR)," ASTM International (2017), https://www.astm.org/d5594-98.html.

37. R. P. D'Amelia, S. Gentile, W. F. Nirode, and L. Huang, "Quantitative Analysis of Copolymers and Blends of Polyvinyl Acetate (PVAc) Using Fourier Transform Infrared Spectroscopy (FTIR) and Elemental Analysis (EA)," *World Journal of Chemical Education* 4 (2016): 25–31, https://doi.org/10.12691/wjce-4-2-1.

38. "ATR-FTIR Library Polymers And Polymer Additives," Shimadzu Scientific Instruments, accessed March 20, 2024, https://store.shimadzu.com.

39. S. Krimm, C. Y. Liang, and G. B. B. M. Sutherland, "Infrared Spectra of High Polymers. II. Polyethylene," *The Journal of Chemical Physics* 25 (1956): 549–562, https://doi.org/10.1063/1.1742963.

40. J. P. Luongo, "Infrared Study of Polypropylene," *Journal of Applied Polymer Science* 3 (1960): 302–309, https://doi.org/10.1002/app.1960.070030907.

41. X. Liu, H. Li, X. Zhao, Y. Chen, and S. Wang, "Comparison of the Corrosion Behavior of Copper Tubes in Formic Acid and Acetic Acid Environment," *Materials and Corrosion* 72 (2021): 1919–1927, https://doi.org/10.1002/maco.202112568.

42. B.-Å. Sultan and E. Sörvik, "Thermal Degradation of EVA and EBA—A Comparison. I. Volatile Decomposition Products," *Journal of Applied Polymer Science* 43 (1991): 1737–1745, https://doi.org/10.1002/app.1991.070430917.

43. T. Manik, M. Sakai, R. S. Situmorang, et al., "Effect of Phosphorus on the Ant-Nest Corrosion Mechanism," *Materials Today Communications* 36 (2023): 106560.

44. P. A. Schweitzer, "Copper and Copper Alloys," in *Fundamentals of Metallic Corrosion* (Boca Raton, FL, USA: Taylor & Francis CRC Press, 2006).

45. A. López-Delgado, E. Cano, J. M. Bastidas, and F. A. López, "A Laboratory Study of the Effect of Acetic Acid Vapor on Atmospheric Copper Corrosion," *Journal of The Electrochemical Society* 145 (1998): 4140–4147, https://doi.org/10.1149/1.1838928.